Cardiovascular Engineering and Technology manuscript No.
(will be inserted by the editor)

Challenges in Modeling Hemodynamics in Cerebral Aneurysms Related to Arteriovenous Malformations

Kimberly A. Stevens Boster · Tanmay C. Shidhore · Aaron A. Cohen-Gadol · Ivan C. Christov · Vitaliy L. Rayz

Received: date / Accepted: date

Abstract *Purpose:* The significantly higher incidence of aneurysms in patients with arteriovenous malformations (AVMs) suggests a strong hemodynamic relationship between these lesions. The presence of an AVM alters hemodynamics in proximal vessels by drastically changing the distal resistance, thus affecting intra-aneurysmal flow. This study discusses the challenges associated with patient-specific modeling of aneurysms in the presence of AVMs.
Methods: We explore how the presence of a generic distal AVM affects upstream aneurysms by examining the relationship between distal resistance and aneurysmal wall shear stress using physiologically realistic estimates for the influence of the AVM on hemodynamics. Using image-based computational mod-

Kimberly A. Stevens Boster (✉)
School of Mechanical Engineering
Purdue University
West Lafayette, Indiana 47907
E-mail: kastevens@purdue.edu

Tanmay C. Shidhore
School of Mechanical Engineering
Purdue University
West Lafayette, Indiana 47907

Aaron A. Cohen-Gadol
Department of Neurological Surgery
Indiana University School of Medicine
Indianapolis, Indiana 46202

Ivan C. Christov
School of Mechanical Engineering
Purdue University
West Lafayette, Indiana 47907

Vitaliy L. Rayz
Weldon School of Biomedical Engineering
School of Mechanical Engineering
Purdue University
West Lafayette, Indiana 47907

els of aneurysms and surrounding vasculature, aneurysmal wall-shear stress is calculated for a range of distal resistances corresponding to the presence of AVMs of various sizes and compared with a control case representing the absence of an AVM.
Results: In the patient cases considered, the alteration in aneurysmal wall shear stress due to the presence of an AVM is considerable, as much as 19 times the base case wall shear stress. Furthermore, the relationship between aneurysmal wall shear stress and distal resistance is shown to be highly geometry-dependent and nonlinear. In most cases, the range of physiologically realistic possibilities for AVM-related distal resistance are so large that patient-specific flow measurements are necessary for meaningful predictions of wall shear stress.
Conclusions: The presented work offers insight on the impact of distal AVMs on aneurysmal wall shear stress using physiologically realistic computational models. Patient-specific modeling of hemodynamics in aneurysms and associated AVMs has great potential for understanding lesion pathogenesis, surgical planning, and assessing the effect of treatment of one lesion relative to another. However, we show that modeling approaches cannot usually meaningfully quantify the impact of AVMs if based solely on imaging data from CT and X-ray angiography, currently used in clinical practice. Based on recent studies, it appears that 4D flow MRI is one promising approach to obtaining meaningful patient-specific flow boundary conditions that improve modeling fidelity.

Keywords image-based modeling · cerebrovascular hemodynamics · arteriovenous malformations · cerebral aneurysms

1 Introduction

The incidence of intracranial aneurysms (IAs) is significantly higher in patients with arteriovenous malformations (AVMs), but the exact cause of the higher incidence rate is unclear [1,2,3]. It has been postulated that a hyperdynamic circulatory state induced by an AVM causes aneurysm formation [2, 3]. This hypothesis is supported by the following two facts. First, the incidence of intracranial aneurysms on arteries feeding an AVM is significantly higher than what is expected in the absence of the AVM. Second, following AVM treatment, in some cases, AVM-related aneurysms have been known to regress. However, the influence of the distal AVM on intra-aneurysmal flow has not been specifically quantified. Not all aneurysms regress following AVM treatment, and the higher aneurysm incidence rate on AVM-feeding arteries alone does not necessarily implicate the hyperdynamic circulatory state.

Understanding the pathogenesis of aneurysms associated with AVMs may have significant clinical implications. Patients with AVMs with associated aneurysms are at greater risk for hemorrhage than patients with AVM alone (7% per year compared to 1.7%) [4]. The higher risk of intracranial hemorrhage indicates that the presence of an AVM-associated aneurysm should be

considered in development of risk stratification models. If a hyperdynamic circulatory state can be linked to prenidal aneurysm formation, models calculating intra-aneurysmal hemodynamics may allow prediction of which prenidal aneurysms are likely to regress following AVM treatment. Though the prevailing theory regarding associated aneurysm pathogenesis relates to the change in intra-aneurysmal hemodynamics induced by a hyperdynamic circulatory state, this theory has not been substantiated, and the exact relationship between changes in distal resistance and proximal hemodynamics has not been previously quantified. Quantifying the impact of distal resistance changes on proximal hemodynamics could lead to a more thorough understanding of AVM-related-aneurysm pathogenesis and could have implications for rupture risk stratification and surgical planning. However, patient-specific modeling of AVM-associated aneurysms presents unique challenges that make this quantification a difficult prospect. In the present work, we first briefly discuss approaches to and challenges with modeling AVMs and aneurysms. Second, we explore the relationship between distal resistance and aneurysmal hemodynamics using typically available clinical data and discuss the implications and limitations of the conclusions which can be drawn from models based on angiographic images.

2 Approaches to Modeling AVM-Associated Aneurysms

Despite the higher incidence of aneurysms in patients with AVMs than in those without, and higher hemorrhage risk associated with the combination, little work has been done to quantify hemodynamic relationship between AVMs and associated aneurysms. Previous approaches exploring the hemodynamic influence of arteriovenous malformations include one-dimensional population-averaged models [5,6], which cannot provide hemodynamic data linked to aneurysm progression (e.g. wall shear stress, [7]). Shakur et al. [8] used quantitative magnetic resonance angiography (MRA) to calculate wall shear stress (WSS) in AVM feeding vessels with and without aneurysms and found significantly higher WSS in feeding vessels with aneurysms. Similarly, feeding vessel WSS has been calculated using *in vivo* phase-contrast MRI flow measurements [9,10]. However, magnetic resonance-based approaches have large uncertainties on velocity gradient-based metrics like WSS [11]. In contrast, image-based computational fluid dynamic (CFD) models can calculate hemodynamic metrics such as WSS with superior resolution, but has not been used to quantify AVM-related hemodynamics. This is, in part, due to the difficulty of resolving the AVM nidus using existing medical imaging technology. The present study attempts to overcome this limitation by coupling three-dimensional high-resolution CFD models with reduced order models representing the distal vasculature, which can be constructed to simulate the presence of an AVM. The present study uses image-based CFD to quantify the change in intra-aneurysmal wall shear stress induced by the presence of an AVM.

Image-based CFD modeling is gaining popularity as a non-invasive technique for cardiovascular flow quantification and has recently gained FDA approval as a diagnostic tool for clinical use [12]. For complex cerebral aneurysms not associated with AVMs, understanding the flow patterns and resulting hemodynamic forces can help diagnostics and treatment planning [13,14,15,16,17,18]. Patient-specific computational models can be generated from data acquired with various imaging modalities, including CTA, MRA and rotational X-ray angiography. Hemodynamic factors such as WSS can be computed with CFD and then used to predict the risk of aneurysm growth and rupture [19,20,21,22,7]. Current approaches for image-based CFD are effective if the model is focused on a single lesion (e.g., an aneurysm) as they typically assume generalized proximal and distal flow conditions; however, if the presence of a second lesion, such as an AVM, significantly changes the flow outside of the modeled region, these traditional approaches for assigning boundary conditions are no longer appropriate.

Determining the patient-specific resistance to flow posed by an AVM is challenging. The tangle of vessels that comprise the AVM cannot be individually resolved *in vivo* with existing medical imaging technology. The net resistance could be calculated from pressure and flow measurements taken at points proximal and distal to the AVM, but such measurements are not routinely acquired in the clinical setting. Cerebrovascular flows are commonly visualized in the clinic with X-ray angiography/digital subtraction angiography (DSA).

A radiopaque contrast agent is injected and imaged as it flows throughout the vasculature, allowing clinicians to visualize blood flow and vascular anatomy. The pixel intensity in the DSA image reflects the changing concentration of contrast, which is influenced by the velocity of the blood flow, which is in turn affected by changes in the distal resistance. However, estimating the resistance from DSA is difficult, considering that the solution to the inverse problem of obtaining velocity from concentration may be non-unique and that the 2D DSA image is a projection of contrast flowing in a 3D volume. Furthermore, the sensitivity of the contrast intensity is low relative to the changes in distal resistance, as shown in Figure 1. DSA images of a patient taken before and after surgical resection of the left cerebellar AVM and clipping of the associated left superior cerebellar artery (SCA) are shown. The aneurysm is clearly visible on the pre-operative image, and completely absent in the post-operative image. The average pixel intensity over time in the region shaded in blue (in Figure 1(a)) is shown in Figure 1(b). The pixel intensity is normalized by the average background pixel intensity. Surgical resection of the AVM changes the distal resistance and flow in the SCA, which may be reflected in the difference in pixel intensity; however, the difference is small, and estimating the change in resistance caused by AVM resection from DSA images alone would be difficult and the resulting values would have large uncertainty.

An alternative modality for measuring blood flow is time-resolved, three-directional phase-contrast MRI (4D flow MRI). Though not yet commonly used in a clinical setting, 4D flow MRI [23], in addition to providing in vivo flow measurements, may also be the answer to the challenge of providing patient-

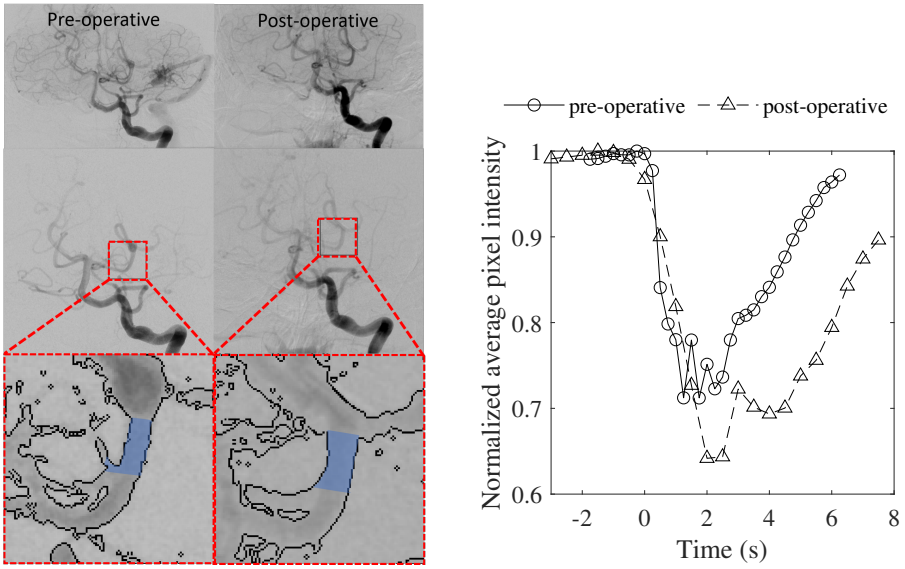

(a) (b)

Fig. 1: (a) A snapshot of digital subtraction angiography data from Patient 3 before and after surgical resection of a left superior cerebellar AVM and clipping of the associated aneurysm on the left superior cerebellar artery. In the subset images, the vessel lumen is outlined in black, and the shaded blue region indicates the area over which the pixel intensity was averaged. (b) Normalized average pixel intensity over time.

specific boundary conditions for image-based CFD models. Although the accuracy of gradient-based hemodynamic metrics like WSS calculated from 4D flow MRI data in cerebral vessels is affected by limitations of its spatial resolution, 4D flow MRI can be used to accurately measure time-resolved flow waveforms at model inlet and outlet locations, which can then be used to generate patient-specific boundary conditions for image-based CFD models. Examples of obtaining flow measurements in AVM-feeding aneursyms can be found in [9], and a pipeline for obtaining flow measurements from 4D flow MR images is described in [24]. Inlet flow profiles can be obtained directly from the 4D flow MRI measurements. The lumped parameter resistance, to be imposed as an outlet boundary condition, can be calculated as

$$R_{out,i} = \frac{\Delta P}{Q_{out,i}} \cdot \frac{\sum_j Q_{out,j}}{\sum_j Q_{in,j}}. \tag{1}$$

Here, $R_{out,i}$ is the resistance at the ith outlet, $Q_{out,i}$ is 4D flow measurement flow rate at each outlet. The ratio of the total flow into and out of the model are included so that the total resistance is consistent with the inlet boundary conditions, if the total flow into and out of the model do not match exactly,

which can happen due to the uncertainty inherent in the measurement system and the fact that some small amounts of flow leave though vessels smaller than 4D flow MRI resolution, such as the side branches of the basilar artery.

Using this approach to create patient-specific models of AVM-associated aneurysms has promise; however, at present, this type of imaging data is not readily available in clinical settings. Therefore, in the second part of this study, we present CFD analyses based on state-of-the-art CTA and X-ray data lacking patient-specific boundary conditions, and demonstrate the shortcomings of this approach in achieving truly patient-specific hemodynamic simulations. Nevertheless, modeling the flow in patient-specific anatomies for a range of physiologically realistic flow conditions, we can draw some important conclusions about the relationship between distal resistance and WSS.

3 Methods

The AVM is an abnormal tangle of vessels (nidus) directly connecting the arterial and venous sides of the circulation, bypassing the capillary bed. Current imaging technology is not capable of resolving individual nidus vessels, making it impossible to create a 3D model of the AVM. Likewise, it is not possible to resolve the flow in each capillary. Therefore, in order to model the effect of changes in distal vasculature (e.g. AVM presence) on intra-aneurysmal flow, all distal vessels, including capillary bed, are modeled as a single lumped parameter at each outlet, representing the total resistance to flow [25]. For each patient, the flow in the aneurysmal arteries with and without a distal AVM were simulated. The influence of the AVM was modeled by reducing the outlet resistance in the artery or arteries feeding the AVM, while maintaining the same inlet flow rate and outlet resistances for arteries not feeding the AVM.

Cerebral aneurysm patients previously treated at the IU Health Neuroscience Center were selected for this retrospective study.The modeling methodology was used to analyze the flow for five patients with AVM-related cerebral aneurysms, listed in Table 1. Patient 2 had multiple aneurysms, but only the aneurysm on the right superior cerebellar artery was considered in the present work since it is the only one affected by the presence of the AVM. CT and X-ray angiography data acquired prior to intervention were anonymized and used to generate 3D surfaces of the aneurysm and surrounding vascular geometries. The images obtained from CT angiograms (CTA) were segmented using open source software ITK-Snap [26] and compared with dynamic rotational X-ray angiography data to eliminate segmentation artifacts. Particular attention was given to regions of special interest, such as the aneurysm neck, an approach which has been shown to yield more accurate segmentation results [27].

The resulting 3D geometry was imported into the open-source modeling platform SimVascular [28], in which the model's inlets and outlets were specified, and a mesh for the fluid domain was generated. SimVascular solves the incompressible Navier–Stokes equations using a solver based on the academic finite element code PHASTA (Parallel, Hierarchical, Adaptive, Stabilized, Tran-

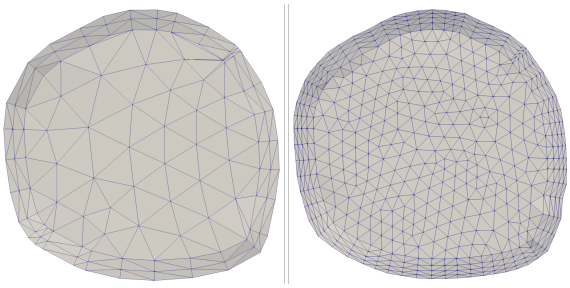

Fig. 2: Examples of the coarsest (left) and finest mesh (right) of the middle cerebral artery (MCA) outlet of Patient 4. A constant boundary layer thickness and ratio (5:1) between the coarse mesh element size and smallest boundary layer mesh element thickness was used in all meshes.

sient Analysis) with the streamline-upwind/Petrov–Galerkin (SUPG) and pressure-stabilizing/Petrov–Galerkin (PSPG) methods, as well as back flow stabilization. 0D-to-3D coupling methods allow for the 3D finite element solver to be coupled to lumped parameter (resistance) models of distant vasculature via boundary conditions. Further details can be found in [28,29,30,31,32]. The models had rigid walls, and Newtonian blood viscosity $\mu = 0.004$ Pa·s and density $\rho = 1060$ kg/m^3 were assumed. In all simulations, a time step of 2.5×10^{-4} s was used (4000 time steps per cardiac cycle). Second-order time integration was used with implicit pressure coupling. Pulsatile physiological flow with a Womersley profile was prescribed at the model's inlets. The flow waveform was based on 4D flow MRI measurements in patients from a different study and scaled so that the cycle-averaged flow rate was consistent with population averages [33,34,35]. Thus, the inlet flow conditions are not "patient-specific," but they are physiologically realistic.

To ensure that the computational results reported herein are mesh independent, results from subsequently refined meshes were compared. In order to achieve mesh resolution sufficiently high for calculating WSS, boundary layer meshing was used, maintaining a constant total boundary layer thickness between meshes (0.0285 cm). The number of elements in the boundary layer was changed to maintain a constant aspect ratio between successive mesh refinements. The ratio of element size for mesh elements in the core of the flow relative to the smallest element in the boundary layer was 5:1. Elements within the boundary layer decreased in thickness radially, where the thickness of each successive element was 80% of the previous element, as shown in Figure 2. For each patient, the mesh was refined by approximately doubling the number of elements until the change in the WSS prediction between simulations on consecutive meshes was less than 5%. Results are shown for the second cardiac cycle since the spatial average of the time-averaged wall shear stress (TAWSS) changed less than 0.2% between the second and third cardiac cycles.

Resistance boundary conditions were assigned at each outlet. Flow in the aneurysmal arteries with and without a distal AVM were simulated. For the AVM-free case, the total peripheral resistance was calculated assuming a total pressure drop of 93 mmHg, then dividing the total pressure drop by the total flow into the model. The total resistance was divided between outlets based on a morphometric relation associating flow and vessel outlet area using the relation

$$R_{out,i} = \frac{\sum_{j=1}^{n} \sqrt{A_j^m}}{\sqrt{A_i^m}} \cdot R_{tot}, \tag{2}$$

where $R_{out,i}$ is the resistance of each outlet, A_i is the outlet area, R_{tot} represents the total resistance of all the outlets, n is the total number of outlets, and m is the morphometric exponent [29,36]. In the present study, $m = 2.4$, based on a range of suggested values and findings that varying the exponent between 2.4 and 2.8 does not significantly impact the WSS [36,37,38,39]. The influence of the AVM was simulated by reducing the outlet resistance in the artery or arteries feeding the AVM, while maintaining the same inlet flow rate and outlet resistances for non-feeding, i.e. not proximal to the AVM, artery outlets. Though it is likely that the AVM was fed by flow from multiple arteries, for the sake of simplicity, the resistance was only altered on the one or two main arteries where a significant amount of flow fed the AVM based on notes made by the attending radiologist and observation of the angiograms.

The rationale for simulating AVM presence with reduced resistance has a physical basis. In Poiseuille flow, the hydrodynamic resistance $R = 8\mu L/(\pi r^4)$ is proportional to the vessel length L and inversely proportional to its radius r^4. Therefore, relative to the AVM-free case, resistance to flow through an AVM (which acts as a shunt) would be reduced. This reduction occurs because the path for flow through an AVM has both decreased distance and increased average radius relative to the path through a capillary bed (the AVM-free case). Clinical measurements also support the idea of reduced resistance. Feeding arteries commonly have increased flow, which would occur due to the relatively reduced resistance in that branch. Further, several studies have reported reduced absolute pressure in the feeding arteries immediately proximal to an AVM and immediate pressure rise with AVM occlusion or embolization [40, 41,42,43,44,45]. The reduced pressure at the AVM entrance reflects the increased flow (larger pressure drop from the heart to the AVM entrance for similar resistance). Clearly, the degree to which the presence of an AVM reduces distal resistance for the aneurysmal arteries depends on the AVM's size, shape, location, interconnectedness, etc. However, predicting resistance based on geometry is impractical given the difficulties in imaging the nidus.

Given the difficulty of obtaining patient-specific resistance estimates from DSA data and in the absence of measured flow and pressure data, which could be used to infer a patient-specific resistance (or reduction in resistance), in the present study, we used resistances based on values reported in the literature. Nornes and Grip reported measurements of the pressure drop and flow in eight cerebral AVMs [45]. Based on their measured values, we estimate lumped

resistance values ranging from 3×10^3 to 8×10^4 g/(cm^4·s) for the eight different AVMs in their study. In the present study, we used resistances of 3×10^3 and 8×10^4 g/(cm^4·s), referred to as "low" and "high" AVM resistances, respectively, at the outlets leading to an AVM. Applying this approach to each patient case allowed us to to bracket a range of reasonable resistance values. Therefore, as many as three flow scenarios were simulated for each patient: one AVM-free case, with resistances distributed using Equation (2), and two cases representing the presence of an AVM. For Patients 1 and 4, the AVM-free feeding artery resistances were lower than the value used for the high-resistance AVM case so no simulation was performed for the high-resistance AVM case. The resistance values used at the feeding artery outlet in the AVM-free case and the percent change in resistance between the AVM-free and AVM-present cases are shown in Table 1. Additionally, for two cases (Patients 3 and 4), a range of resistance values (1/2, 1/4, 1/10, and 1/20 of the AVM-free case's resistance) was prescribed to explore the relationship between reduced resistance and WSS – a metric linked to aneurysm progression and rupture.

4 Results and Discussion

The WSS magnitude distribution at peak systole is shown in Figure 3 for each patient's model, along with inserts showing the details of the WSS distribution specifically on the aneurysm. In all patients, the WSS on the modeled vasculature is demonstrably higher in the AVM case than the AVM-free case. The numerical value of TAWSS magnitude, which is further spatially averaged over the entire aneurysm, is given in Table 1. Decreasing the feeding artery outlet resistance increased the flow rate and increased TAWSS over the aneurysm. This is of particular note for Patient 1, where the aneurysm is located on the contralateral side from the AVM. In this case, the increased flow towards the AVM caused an increase in WSS for an aneurysm located on the contralateral side. The increased WSS on the contralateral aneurysm occurs because the decreased resistance in the MCA causes additional flow to be re-routed through the ACOM. As can be seen in 3a, the aneurysm is located right at the junction of the left ACA and the ACOM, and thus, the increased flow in the ACOM causes increased WSS on the aneurysm, even though flow in the left ACA is decreased. This can be seen in the plots of WSS in 3a, where the ACOM has demonstrably increased WSS in the AVM present case. This result emphasizes the importance of image-based flow analysis, which can provide important quantifiable insight into flow in AVM-related aneurysms that cannot be gained from mere observation, intuition, or simplified models alone.

In most cases in which both a high and low AVM resistance value were used, the difference in TAWSS between the high and low AVM resistances is considerable, with low resistance TAWSS values two to six times that of the high resistance case (Table 1). The range is so large that bracketing a range of WSS values using a reasonable range of resistance values provides relatively

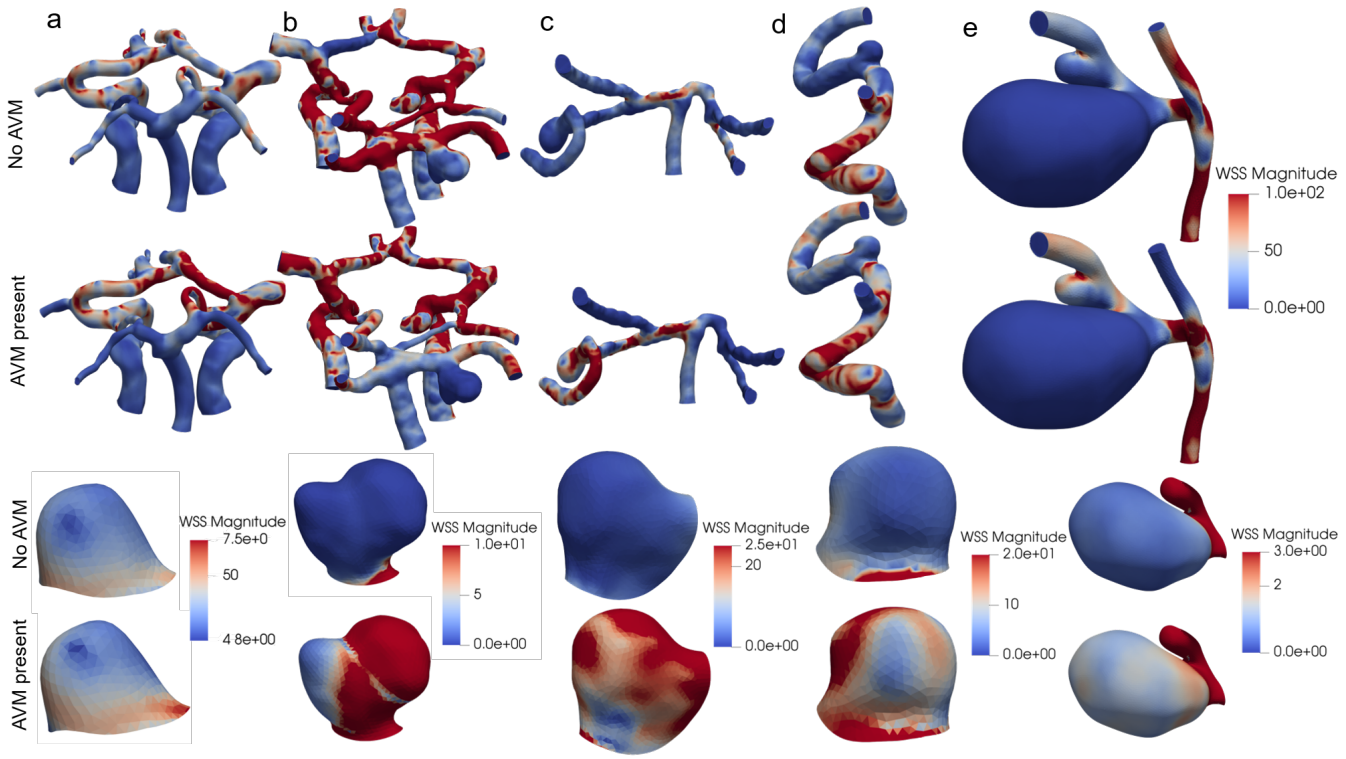

Fig. 3: Magnitude of the wall shear stress (WSS, in dynes/cm^2) at peak systole for each patient (a-e). (Patients 1–5 are shown left to right.) The top two rows show the entire computational domain, with the AVM-free case shown on the top row, and the low-resistance AVM case shown on the second row. The bottom two rows show the WSS magnitude specifically on the aneurysm, with the AVM-free and AVM cases on the second from bottom and bottom rows, respectively.

little information about the magnitude of WSS, though it can indicate the direction and presence of WSS change. Therefore, in order to predict the degree to which a change in resistance (either due to AVM presence or AVM treatment) would effect WSS, patient-specific data for flow and pressure are needed to more accurately estimate the outlet resistance. However, one notable exception to this requirement is observed in Patient 1, where, even with the wide range of resistance values used in this study the change in WSS is relatively modest relative to the AVM-free case (22%). Thus, even without knowing the resistance for this particular patient, we can conclude that the change in WSS in this aneurysm is unlikely to be large.

Decreasing the distal resistance at the outlet corresponding to the AVM's feeding artery, causes increased flow, and therefore increased WSS throughout the same artery. In order to account for this increase, the WSS in the aneurysm is normalized by the AVM's feeding artery systolic WSS. Except for ACA aneurysm in Patient 1, the AVM's feeding artery is also the aneurysm parent vessel. Thus, except for Patient 1, the percent change in normalized TAWSS is lower than the non-normalized case (see Table 1). The percent change in normalized WSS represents the increase of wall shear stress in the aneurysm, in addition to the change expected due to overall increased flow. While the percent change is generally lower in the normalized case, the magnitude of that change varies considerably from patient to patient and between the high and low resistance cases, thus highlighting the need for resistance values based on patient-specific measurements. However, it is interesting to note that even with the wide range of resistance values considered in this work, the WSS in the aneurysm increased more than the WSS in the feeding vessel, as illustrated by the positive percent change in the normalized WSS.

For Patient 1, the aneurysm and its parent vessel are located on the contralateral side from the AVM and its feeding artery. In this case, the normalized aneurysm WSS actually decreases from the AVM-free case to the low resistance case, since the feeding artery WSS increases more than the aneurysm WSS (resulting in a negative percent change between the AVM-free and low resistance case, see Table 1). This is unsurprising, since the flow through the aneurysm's parent vessel on the contralateral side would not change as much as the flow through the feeding artery.

To explore the relationship between resistance and WSS, we systematically varied the distal resistance for two patients (3 and 4). Figure 4 shows the ratio of the TAWSS for the AVM-free case to the TAWSS for the AVM-present case, as a function of the feeding artery resistance normalized by the AVM-free case resistance. The feeding artery flow rate for the AVM-free cases divided by the AVM-present case is also shown. The relationship between feeding artery flow rate and resistance is inversely linear, i.e. $Q \propto 1/R$. Since the distal resistance is much larger than the proximal resistance, the distal resistance dominates the division of flow between the outlets. Therefore, flow to each outlet Q can be estimated based solely on the distal resistances. The ratio of the flow rates for the AVM-free and AVM-present cases $[Q_N/Q]_{pred}$ that would occur in this

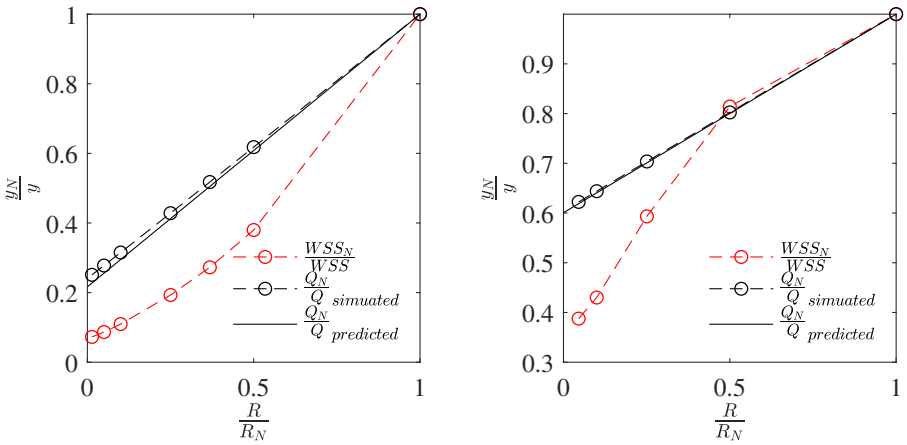

(a) Patient 3 (b) Patient 4

Fig. 4: Feeding artery flow rate Q and aneurysm TAWSS and for the "AVM-free" case divided by AVM case as a function of the AVM resistance divided by the AVM-free resistance, i.e. $\text{TAWSS}_N/\text{TAWSS}$ and Q_N/Q as functions of R/R_N, illustrating that resistance and flow are inversely linearly related, as expected. However, the WSS and resistance/flow are not linearly related. Markers/dashed lines are from simulation; the solid line is the expected flow if the flow split is determined based solely on the outlet resistance.

Pt #	aneurysm location	AVM location	feeding artery	feeding artery resistance no-AVM case ($g/cm^4 \cdot s$)	% change resistance		Aneurysm TAWSS ($dyne/cm^2$)			Feeding Artery Systolic WSS ($dyne/cm^2$)			Aneurysm TAWSS normalized			% change TAWSS normalized		% change TAWSS	
					high	low	no AVM	high	low	no AVM	high	low	no AVM	high	low	high	low	high	low
1	L ACA	R frontal lobe	R MCA	2.30×10^4	NA	87	12	NA	15	48	NA	77	0.25	NA	0.19	NA	−23	NA	22
2	R SCA	R cerebellar	L SCA, R SCA	3.16×10^5, 1.62×10^5	75	99	1	3	19	59	101	314	0.02	0.03	0.06	56	242	165	1708
3	L SCA	L cerebellar	L SCA	2.17×10^5	63	99	4	13	50	7	15	39	0.54	0.90	1.29	67	141	267	1277
4	R MCA	R parietal	R MCA	6.58×10^4	NA	95	5	NA	12	20	NA	39	0.24	NA	0.32	NA	34	NA	158
5	L ACA	L frontal	L ACA	1.12×10^5	29	97	2	3	5	30	34	54	0.07	0.08	0.09	7	24	23	125

Table 1: Quantitative summary of the computational results for all patients analyzed in this case study. Flow scenario (AVM-free, high, or low AVM) is indicated by "no AVM," "high," and "low." Percent change is the change between the no AVM case and the AVM-present cases. The aneurysm TAWSS is normalized by the feeding artery systolic WSS. "NA" stands for "not applicable."

case is plotted with the solid lines. Here,

$$\left[\frac{Q_N}{Q}\right]_{pred} = \frac{R_o + R_N \cdot R/R_N}{R_o + R_N}, \tag{3}$$

where R_o is the total resistance for all other outlets, R_N is the resistance of the feeding artery outlet in the AVM-free case, and R is the resistance of the feeding artery outlet in the AVM cases. The good agreement between the AVM feeding artery flow rate from simulation (markers) and that predicted based on the distal resistances (solid lines) indicates that that the impact of the proximal resistance on flow division is minimal.

In contrast, the relationship between AVM feeding artery resistance and aneurysmal WSS is nonlinear. Decreasing the distal resistance (representing the presence of an AVM) increases aneurysm WSS, as expected. However, we observed that the change in TAWSS is not directly proportional to parent vessel flow rate or parent vessel distal resistance. This discrepancy is a notable observation from our study because, for Poiseuille flow in a circular channel, we have TAWSS $= (4\mu/\pi r^3) \cdot Q$ (a direct proportionality). Thus, one might expect a linear relationship between flow and the WSS. Furthermore, not only is the relationship between resistance and WSS nonlinear, the shape of this curve varies considerably between Patients 3 and 4. Therefore, we highlight the need for patient-specific models to predict how WSS will respond to changes in resistance and flow.

Many modeling studies use a morphometric relation associating vessel flow and vessel area after branching (e.g. a "generalized" Murray's Law) to distribute outlet resistance values [36,29,46,47,48,21,20,37,38,39]; however, this would not be appropriate in the presence of an AVM, where the short-circuiting shunt can drastically alter normal flow patterns. As mentioned above, patient-specific flow and pressure measurements can be obtained using catheter-based instruments [49] or using 4D flow MRI [50], which can then be used to estimate appropriate outlet resistance conditions. With pressure and flow measurements obtained at points located proximally and distally to an AVM, one could easily estimate a lumped parameter resistance value for the AVM which, even with large measurement uncertainty, would be considerably more precise than a range of resistance values drawn from a population of AVM patients. Therefore, in most cases, patient-specific flow and pressure data are necessary to predict with any degree of precision how outlet resistance from distal AVM presence or removal will change WSS.

Besides the small sample size, this study has some limitations. The boundary conditions assigned were physiologially realistic, but by no means patient-specific. Though the geometries modeled came from patients with AVM-related aneurysms, and the AVM-feeding arteries were included in the models and assigned reduced resistance representing the influence of a distal AVM, the degree of resistance reduction in each patient was unknown and therefore a range of resistances was assigned based on values found in the literature. Likewise, the inlet flows were assigned based on waveforms derived from patients without

AVMs, and scaled so that the total flow matched population averages reported in the literature. The outlet boundary conditions for the arteries not feeding the AVM (and the arteries in the AVM-free case) were based on morphometric scaling laws, which have been shown to approximate the true resistance; therefore, these outlet conditions cannot be truly considered patient-specific. Thus, the calculations and conclusions cannot provide insight pertaining to the patients from which the geometries were obtained. However, since the input conditions are physiologically realistic, the results are physiologically relevant, and the conclusions, regarding the need for patient-specific boundary conditions and the nonlinear relationship between resistance and wall shear stress can provide insight for researchers carrying out patient-specific modeling of AVM-related aneurysms.

Another limitation of the study is the idealized treatment of the AVM and other distal vasculature, lumping them into a single resistance value. While it is well known that both AVMs and healthy distal vasculature have some degree of compliance that can change the flow and pressure wave form [51], inclusion of the compliance is only expected to change the temporal form of the pressure, flow, and WSS waveforms, and not the time-averaged quantities. This was verified on one of the present models, in which physiologically realistic RCR outlet boundary conditions were applied. The temporal variation in WSS changed relative to the resistance-only case, but the time-averaged WSS changed negligibly; the change in time-averaged WSS due to the introduction of distal compliance was smaller than the uncertainty associated with grid refinement (less than 5%). Due to the difficulty of estimating AVM compliance, it was determined that a resistance-only outlet boundary condition was preferable. However, it seems possible that with dynamic flow information, which could be obtained from, say, 4D flow MRI, the lumped compliance of the AVM and distal vasculature could be estimated in a patient-specific way.

5 Conclusion

The hemodynamic impact of arterivenous malformations (AVMs) on proximal cerebral aneurysms was quantified using image-based modeling for 5 patients. As expected, changing the distal resistance influences aneurysm wall shear stress (WSS). However, the degree to which distal resistance influences the WSS appears to be geometry-dependent, requiring detailed flow analysis to make predictions for each patient. Importantly, we found that the relationship between WSS and flow distribution is nonlinear. Therefore, image-based modeling is required to predict the relationship between WSS and distal resistance, and patient-specific boundary conditions are essential for predicting the WSS magnitude.

More work is needed to definitively answer the question of aneurysm pathogenesis; however, the results from our case studies support the hypothesis that AVM presence may cause flow conditions that are associated with an increased risk of cerebral aneurysm initiation and progression [21,20,7]. More impor-

tantly, our study demonstrates that assigning outflow boundary conditions without patient-specific flow information is not appropriate for hemodynamics in aneurysms with associated AVMs and, in addition to patient-specific geometries, patient-specific *boundary conditions* are also required. 4D flow MRI is a promising approach that could potentially be used to obtain such patient-specific boundary conditions.

Though the challenges inherent in incorporating the effect of AVMs in patient-specific modeling are significant, we believe that there is significant potential in developing an approach towards patient-specific modeling that can provide insight for clinical decision-making regarding treatment of AVMs and aneurysms, e.g. regarding which lesion should be treated first, or for predicting the impact of a particular AVM treatment on an aneurysm located elsewhere in the brain. Although in the cases explored in the present work, WSS increased with reduced distal resistance, meaning that increasing resistance due to AVM treatment leads to reduced shear stress, this trend will not always hold. For example, a contralaterally located aneurysm may be subjected to higher WSS following AVM treatment/increased distal resistance if extra flow were to be diverted through the contralaterally located aneurysm. Once adapted for the influence of AVMs, patient-specific modeling can be used to answer the latter and related cerebrovascular hemodynamics questions.

Acknowledgements K.A.S.B. was supported in part by the Lillian Gilbreth Postdoctoral Fellowship from Purdue's College of Engineering. K.A.S.B. and I.C.C. additionally received partial support from the US National Science Foundation under grant No. CBET-1705637.

Conflict of interest

Kimberly Boster, Tanmay Shidhore, Aaron Cohen-Gadol, Ivan Christov, and Vitaliy Rayz declare that they have no conflict of interest.

References

1. S.K. Rammos, B. Gardenghi, C. Bortolotti, H.J. Cloft, G. Lanzino, American Journal of Neuroradiology **37**(11), 1966 (2016). DOI 10.3174/ajnr.A4869
2. G. Redekop, K. TerBrugge, W. Montanera, R. Willinsky, Journal of Neurosurgery **89**(4), 539 (1998). DOI 10.3171/jns.1998.89.4.0539
3. M. Tanaka, in *Brain Arteriovenous Malformations: Pathogenesis, Epidemiology, Diagnosis, Treatment and Outcome*, ed. by V. Benes, O. Bradac (Springer International Publishing, Cham, 2017), pp. 5–22. DOI 10.1007/978-3-319-63964-2{_}2
4. R.D. Brown, D.O. Wiebers, G.S. Forbes, Journal of Neurosurgery **73**(6), 859 (1990). DOI 10.3171/jns.1990.73.6.0859
5. E. Gao, W.L. Young, E. Ornstein, J. Pile-Spellman, M. Qiyuan, Journal of Cerebral Blood Flow & Metabolism **17**(8), 905 (1997). DOI 10.1097/00004647-199708000-00009
6. E. Gao, W.L. Young, J. Pile-Spellman, S. Joshi, H. Duong, P.E. Stieg, Q. Ma, Neurosurgery **41**(6), 1345 (1997). DOI 10.1097/00006123-199712000-00020
7. J. Frösen, J. Cebral, A.M. Robertson, T. Aoki, Neurosurgical Focus **47**(1), E21 (2019). DOI 10.3171/2019.5.FOCUS19234

8. S.F. Shakur, S. Amin-Hanjani, H. Mostafa, F.T. Charbel, A. Alaraj, Stroke **46**(7), 1997 (2015). DOI 10.1161/STROKEAHA.115.009545
9. S. Ansari, S. Schnell, T. Carroll, P. Vakil, M. Hurley, C. Wu, J. Carr, B. Bendok, H. Batjer, M. Markl, American Journal of Neuroradiology **34**(10), 1922 (2013). DOI 10.3174/ajnr.A3537
10. W. Chang, M.W. Loecher, Y. Wu, D.B. Niemann, B. Ciske, B. Aagaard-Kienitz, S. Kecskemeti, K.M. Johnson, O. Wieben, C. Mistretta, P. Turski, American Journal of Neuroradiology **33**(8), 1565 (2012). DOI 10.3174/ajnr.A3010
11. L. Boussel, V. Rayz, A. Martin, G. Acevedo-Bolton, M.T. Lawton, R. Higashida, W.S. Smith, W.L. Young, D. Saloner, Magnetic Resonance in Medicine **61**(2), 409 (2009). DOI 10.1002/mrm.21861
12. C.A. Taylor, T.A. Fonte, J.K. Min, Journal of the American College of Cardiology **61**(22), 2233 (2013). DOI 10.1016/j.jacc.2012.11.083
13. V.L. Rayz, M.T. Lawton, A.J. Martin, W.L. Young, D. Saloner, Journal of Biomechanical Engineering **130**(2), 021004 (2008). DOI 10.1115/1.2898833
14. V. Rayz, L. Boussel, M. Lawton, G. Acevedo-Bolton, L. Ge, W. Young, R. Higashida, D. Saloner, Annals of Biomedical Engineering **36**(11), 1793 (2008). DOI 10.1007/s10439-008-9561-5
15. V.L. Rayz, A. Abla, L. Boussel, J.R. Leach, G. Acevedo-Bolton, D. Saloner, M.T. Lawton, Annals of Biomedical Engineering **43**(5), 1210 (2015). DOI 10.1007/s10439-014-1170-x
16. A. Vali, A.A. Abla, M.T. Lawton, D. Saloner, V.L. Rayz, Journal of Biomechanics **50**, 195 (2017). DOI 10.1016/j.jbiomech.2016.11.028
17. L. Boussel, V. Rayz, C. McCulloch, A. Martin, G. Acevedo-Bolton, M. Lawton, R. Higashida, W.S. Smith, W.L. Young, D. Saloner, Stroke **39**(11), 2997 (2008). DOI 10.1161/STROKEAHA.108.521617
18. V.L. Rayz, L. Boussel, L. Ge, J.R. Leach, A.J. Martin, M.T. Lawton, C. McCulloch, D. Saloner, Annals of Biomedical Engineering **38**(10), 3058 (2010). DOI 10.1007/s10439-010-0065-8
19. H. Meng, V.M. Tutino, J. Xiang, A. Siddiqui, American Journal of Neuroradiology **35**(7), 1254 (2014). DOI 10.3174/ajnr.A3558
20. F.J. Detmer, B.J. Chung, F. Mut, M. Slawski, F. Hamzei-Sichani, C. Putman, C. Jiménez, J.R. Cebral, International Journal of Computer Assisted Radiology and Surgery **13**(11), 1767 (2018). DOI 10.1007/s11548-018-1837-0
21. J. Cebral, E. Ollikainen, B. Chung, F. Mut, V. Sippola, B. Jahromi, R. Tulamo, J. Hernesniemi, M. Niemelä, A. Robertson, J. Frösen, American Journal of Neuroradiology **38**(1), 119 (2017). DOI 10.3174/ajnr.A4951
22. G. Zhou, Y. Zhu, Y. Yin, M. Su, M. Li, Scientific Reports **7**(1), 5331 (2017). DOI 10.1038/s41598-017-05886-w
23. M. Markl, A. Frydrychowicz, S. Kozerke, M. Hope, O. Wieben, Journal of Magnetic Resonance Imaging **36**(5), 1015 (2012). DOI 10.1002/jmri.23632
24. M. Aristova, A. Vali, S.A. Ansari, A. Shaibani, T.D. Alden, M.C. Hurley, B.S. Jahromi, M.B. Potts, M. Markl, S. Schnell, Journal of Magnetic Resonance Imaging **50**(6), 1718 (2019). DOI 10.1002/jmri.26784
25. A.L. Marsden, M. Esmaily-Moghadam, Applied Mechanics Reviews **67**(3), 030804 (2015). DOI 10.1115/1.4029909
26. P.A. Yushkevich, J. Piven, H.C. Hazlett, R.G. Smith, S. Ho, J.C. Gee, G. Gerig, NeuroImage **31**(3), 1116 (2006). DOI 10.1016/j.neuroimage.2006.01.015
27. P. Berg, S. Voß, S. Saalfeld, G. Janiga, A.W. Bergersen, K. Valen-Sendstad, J. Bruening, L. Goubergrits, A. Spuler, N.M. Cancelliere, D.A. Steinman, V.M. Pereira, T.L. Chiu, A.C.O. Tsang, B.J. Chung, J.R. Cebral, S. Cito, J. Pallarès, G. Copelli, B. Csippa, G. Paál, S. Fujimura, H. Takao, S. Hodis, G. Hille, C. Karmonik, S. Elias, K. Kellermann, M.O. Khan, A.L. Marsden, H.G. Morales, S. Piskin, E.A. Finol, M. Pravdivtseva, H. Rajabzadeh-Oghaz, N. Paliwal, H. Meng, S. Seshadhri, M. Howard, M. Shojima, S.i. Sugiyama, K. Niizuma, S. Sindeev, S. Frolov, T. Wagner, A. Brawanski, Y. Qian, Y.A. Wu, K.D. Carlson, D. Dragomir-Daescu, O. Beuing, Cardiovascular Engineering and Technology **9**(4), 565 (2018). DOI 10.1007/s13239-018-00376-0
28. A. Updegrove, N.M. Wilson, J. Merkow, H. Lan, A.L. Marsden, S.C. Shadden, Annals of Biomedical Engineering **45**(3), 525 (2017). DOI 10.1007/s10439-016-1762-8

29. H. Lan, A. Updegrove, N.M. Wilson, G.D. Maher, S.C. Shadden, A.L. Marsden, Journal of Biomechanical Engineering **140**(2), 245011 (2018). DOI 10.1115/1.4038751
30. C.H. Whiting, K.E. Jansen, International Journal for Numerical Methods in Fluids **35**(1), 93 (2001). DOI 10.1002/1097-0363(20010115)35:1⟨93::AID-FLD85⟩3.0.CO;2-G
31. M. Esmaily Moghadam, Y. Bazilevs, T.Y. Hsia, I.E. Vignon-Clementel, A.L. Marsden, Computational Mechanics **48**(3), 277 (2011). DOI 10.1007/s00466-011-0599-0
32. M. Esmaily Moghadam, I.E. Vignon-Clementel, R. Figliola, A.L. Marsden, Journal of Computational Physics **244**, 63 (2013). DOI 10.1016/j.jcp.2012.07.035
33. M.E. MacDonald, R. Frayne, Physiological Measurement **36**(7), 1517 (2015). DOI 10.1088/0967-3334/36/7/1517
34. M. Zhao, S. Amin-Hanjani, S. Ruland, A. Curcio, L. Ostergren, F. Charbel, American Journal of Neuroradiology **28**(8), 1470 (2007). DOI 10.3174/ajnr.A0582
35. L. Zarrinkoob, K. Ambarki, A. Wåhlin, R. Birgander, A. Eklund, J. Malm, Journal of Cerebral Blood Flow & Metabolism **35**(4), 648 (2015). DOI 10.1038/jcbfm.2014.241
36. J. Seo, D.E. Schiavazzi, A.M. Kahn, A.L. Marsden, International Journal for Numerical Methods in Biomedical Engineering **36**(8), e3351 (2020). DOI 10.1002/cnm.3351
37. Y. Zhou, G.S. Kassab, S. Molloi, Physics in Medicine and Biology **44**(12), 2929 (1999). DOI 10.1088/0031-9155/44/12/306
38. S. Rossitti, J. Löfgren, Stroke **24**(3), 371 (1993). DOI 10.1161/01.STR.24.3.371
39. C. Francis, L. Frederic, L. Sylvie, P. Prasanna, D. Henri, Microcirculation **16**(4), 331 (2009). DOI 10.1080/10739680802662607
40. G. Duckwiler, J. Dion, F. Vinuela, B. Jabour, N. Martin, J. Bentson, American Journal of Neuroradiology **11**(1), 169 (1990)
41. P. Fogarty-Mack, J. Pile-Spellman, L. Hacein-Bey, A. Osipov, J. DeMeritt, E.C. Jackson, W.L. Young, American Journal of Neuroradiology **17**(8), 1443 (1996)
42. C.A. Jungreis, J.A. Horton, American Journal of Neuroradiology **10**(5), 1057 (1989). URL http://www.ajnr.org/content/10/5/1057.abstract
43. C.A. Jungreis, J.A. Horton, S.T. Hecht, American Journal of Neuroradiology **10**(3), 575 (1989). URL http://www.ajnr.org/content/10/3/575.abstract
44. R.F. Spetzler, R.W. Hargraves, P.W. McCormick, J.M. Zabramski, R.A. Flom, R.S. Zimmerman, Journal of Neurosurgery **76**(6), 918 (1992). DOI 10.3171/jns.1992.76.6.0918
45. H. Nornes, A. Grip, Journal of Neurosurgery **53**(4), 456 (1980). DOI 10.3171/jns.1980.53.4.0456
46. J. Sturdy, J.K. Kjernlie, H.M. Nydal, V.G. Eck, L.R. Hellevik, Journal of Computational Science **31**, 137 (2019). DOI 10.1016/j.jocs.2019.01.004
47. A.G. van der Giessen, H.C. Groen, P.A. Doriot, P.J. de Feyter, A.F. van der Steen, F.N. van de Vosse, J.J. Wentzel, F.J. Gijsen, Journal of Biomechanics **44**(6), 1089 (2011). DOI 10.1016/j.jbiomech.2011.01.036
48. M. McElroy, A. Keshmiri, Proceedings of the Institution of Mechanical Engineers, Part H: Journal of Engineering in Medicine **232**(2), 103 (2018). DOI 10.1177/0954411917699237
49. M. Levitt, P. McGah, A. Aliseda, P. Mourad, J. Nerva, S. Vaidya, R. Morton, B. Ghodke, L. Kim, American Journal of Neuroradiology **35**(1), 143 (2014). DOI 10.3174/ajnr.A3624
50. J. Zhang, S. Bhattacharya, P.P. Vlachos, Experiments in Fluids **61**(6), 131 (2020). DOI 10.1007/s00348-020-02974-y
51. S.F. Shakur, S. Amin-Hanjani, M. Abouelleil, V.A. Aletich, F.T. Charbel, A. Alaraj, Neurological Research **39**(1), 7 (2017). DOI 10.1080/01616412.2016.1258970